A three-layer-mesh bridging domain for coupled atomistic–continuum simulations at finite temperature: Formulation and testing

CrossMark

Alireza Sadeghirad *, Feng Liu

Department of Materials Science and Engineering, University of Utah, Salt Lake City, UT 84112, USA

A R T I C L E   I N F O

A B S T R A C T

Although concurrent multiscale methods have been well developed for zero-temperature simulations, improvements are needed to meet challenges pertaining to finite-temperature simulations. Bridging domain method (BDM) is one of the most efficient and widely-used multiscale atomistic–continuum techniques. It is recently revealed that the BDM coupling algorithm has a cooling effect on the atoms in the bridging domain (BD), and application of thermostats to rectify the cooling effect in the original BDM formulation is unstable. We propose improvement of the BDM formulation for finite-temperature simulations by employing a three-layer mesh structure in the BD, consisting of coarse, meso, and atomic meshes. The proposed method uses a mesh-independent physics-based discrimination between thermal and mechanical waves to define and introduce a meso mesh that is independent of the finite-element (FE) mesh. Temperature stability in the BD is achieved by constraining only the mechanical part of atomic motion to the FE displacements while unconstrained thermal vibrations are thermostatted using local thermostats in the BD. The new architecture of three-layer-mesh BD effectively mitigates the temperature cooling effect encountered by the conventional BDM as well as suppresses the spurious mechanical wave reflection. Numerical simulations have shown the robustness and accuracy of the proposed multiscale method at finite temperature.

© 2013 Elsevier B.V. All rights reserved.

1. Introduction

Over the past few decades, computation has firmly established itself as a new approach in parallel to experiment and theory in understanding fundamental materials properties. Using supercomputers, which are accessible widely to academic community today, it is possible to carry out first-principles simulations of hundreds of atoms for tens of picoseconds and molecular dynamics (MD) simulations with interatomic potentials of millions of atoms for microseconds. However, these accessible length and time scales are still far short of the length scale and especially the time scale of real experiments. Some properties, for which convergence is very fast, e.g. those of point defects in periodic crystals, can be accurately calculated using first-principles techniques. However, the so-called strongly coupled multiscale systems have the properties whose convergence is very slow. These systems are typically associated with a long-range interaction, either electrostatic or elastic. As such, a process, which takes place in a small region, can be affected by the collective behavior of a very large number of atoms over long, sometimes even macroscopic distances. Also, in some cases, the detailed interactions of certain key atoms can influence the equilibrium configuration of potentially tens of thousands of atoms. Concurrent multiscale methods have

---

* Corresponding author. Tel.: +1 801 831 5971; fax: +1 801 581 4816.
 E-mail address: alireza.sadeghirad@utah.edu (A. Sadeghirad).

been developed to circumvent the temporal and spatial limitations of all-atom simulations for modeling strongly coupled multiscale systems, in which the critical zones are limited to small parts of the problem domain while continuum description elsewhere. The fact that it is often unnecessary to use all-atom simulations to treat the whole problem domain is another motivation toward multiscale modeling. Processes involving bond formation, bond breaking, charge transfer, and nonlinear response are best handled with quantum/molecular mechanics while large and arbitrary geometries with wide-ranging boundary conditions can be readily handled with continuum mechanics [1].

The key to multiscale methods is to have an accurate and efficient algorithm that bridges seamlessly different scales. While sequential multiscale methods have enjoyed long-time success [2]; concurrent multiscale methods have been more challenging, as they need to adress a number of issues associated with energy transmission and changes in the constitutive description of a material across the interface between different models, such as spurious wave reflection. Different concurrent multiscale methods have been developed so far, including the quasicontinuum method (QM) [3,4], coarse-grained MD method (CGMD) [5,6], macroscopic–atomistic–ab initio dynamics (MAAD) method [7,8], bridging scale method (BSM) [9,10], bridging domain method (BDM) [11,12], and concurrent atomistic to continuum (AtC) coupling method [13]. In the QM, the entire model is viewed as an atomistic model while representative atoms and the Cauchy–Born rule are used to compute strain energy without using fully atomistic resolution everywhere. To eliminate the unnecessary atomistic degrees of freedom, representative atoms are selected to define finite elements for which the mechanical variables are calculated using finite-element (FE) interpolation and the Cauchy–Born rule. Accurate computation of the energy requires that the atoms be coincident with the finite element nodes in the critical fully-atomistic subdomain. Similarly, in the multiscale CGMD method, critical regions of the system are modeled with MD, while elsewhere is coarse grained for efficiency. The CGMD equations of motion smoothly match those of MD as the mesh size is reduced to the atomic scale since they are derived directly from finite-temperature MD through a statistical coarse graining procedure. In this method, the cross-over to atomistic domain for atomic-sized cells is completely smooth and no handshaking region between MD and CGMD regions is required. The MAAD couples a tight-binding (TB) quantum mechanics approximation with MD and in turn with a FE continuum model. In this method, atomistic and continuum models are coupled in a handshaking domain in which the two Hamiltonians are averaged. To reduce spurious reflections into the MD zone and to thermalize high-frequency phonons propagating through regions where the mesh spacing changes, the FE degrees of freedom are weakly coupled to a Brownian heat bath i.e. the random and dissipative terms are added to their equations of motion. The BSM couples MD and FE models without the need to mesh down the continuum model to the atomic scale by decomposing the displacement field into coarse and fine scales. It also eliminates the unwanted MD degrees of freedom by accounting for them in the form of an impedance force augmenting the standard MD equations of motion, so that high frequency waves which cannot be resolved by the FE model are dissipated naturally out of the MD region.

The concurrent multiscale methods have been mostly applied to study mechanics problems such as crack nucleation/propagation and crystal plasticity. One of the most popular multiscale methods is the BDM [11,12], which has been used in a number of interesting mechanics simulations [14–20]. The BDM is an overlapping domain decomposition scheme in which displacement/velocity compatibility between the atomistic and continuum domains is imposed using the Lagrange multipliers technique. In this regard, the BDM is similar to the earlier Arlequin method [21–24], which couples continuum models. In the BDM, similar to the BSM, the continuum model is not meshed down to the atomic scale since the positions of atoms and nodes are not necessarily identical in the BD. A uniform continuum mesh can be used, which does not correspond with atomic positions. To increase the efficiency, large finite elements can be used within the smoothly discretized meshes, without encountering the issues associated with rapid element-size changes. The BDM uses a so-called BD to couple MD and finite element (FE) models. Consequently, the quantities associated with the atoms and FE nodes need to be transferred between different models only in the BD. In this regard, the BDM is advantageous over the BSM, in which the FE mesh spans over the whole MD zone. Recently, an absorbing boundary condition [25] has been developed that enables application of the BDM with smaller bridging zones to further increase its efficiency. The BDM uses an effective but inexpensive algorithm [26] to remove spurious wave reflections whereas some other techniques [27–30,9] use computationally expensive time history kernels to obtain reflectionless boundary conditions. Furthermore, the BDM generally employs a linear scaling of the energies in the BD, in which the atomistic (continuum) energy is dominant near the purely atomistic (continuum) domain. This strategy provides a gradual transition from the molecular model to the continuum model, and alleviates the error that arises from dropping the atomistic energies from far-field atoms. Also, the BDM can be applied to nonlinear problems since it is not based on linearization.

In the BDM, the system is partitioned into three sub-domains (Fig. 1): atomistic, continuum, and BD. Displacement/velocity compatibility between atomistic and continuum scales in the BD is imposed using the Lagrange multipliers technique. The compatibility can be imposed stringently by associating one Lagrange multiplier with each degree of freedom of each atom in the BD, or it can be applied weakly by approximating the Lagrange multipliers from the finite element mesh i.e. one Lagrange multiplier is associated with each degree of freedom of each FE-node in the BD [12,17]. Application of L^2 and H^1 couplings in the BDM formulation has been investigated in [31,32]. It is found that L^2 coupling with a piecewise linear weight function, such as that used in this paper, is stable. One important step in the BDM is to diagonalize the Lagrange-multipliers constraint matrix using the row-sum technique, which is essential in eliminating spurious wave reflections at the interface of the atomistic and continuum domains [26]. The diagonalization step has also a positive side effect of reducing computational cost. According to use of the Lagrange multipliers in the BDM formulation, total Hamiltonian is divided into three parts: atomistic Hamiltonian, continuum Hamiltonian, and the Hamiltonian associated with the Lagrange multipliers.
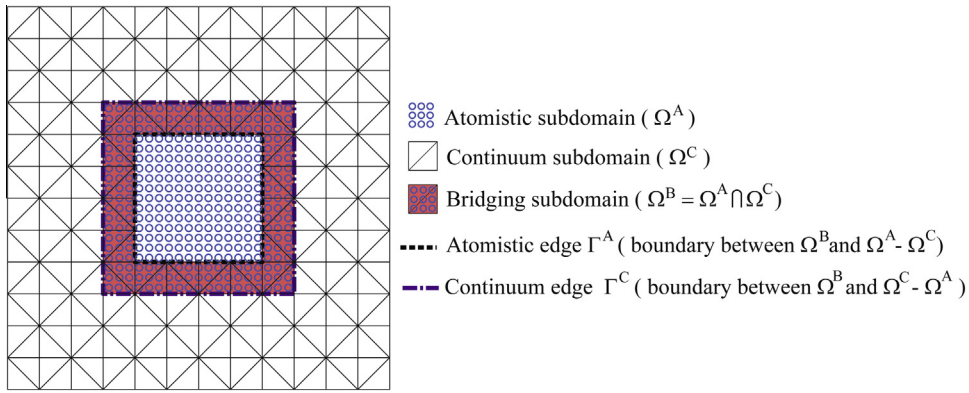
Fig. 1. Illustration of three sub-domains in a BDM simulation: atomistic, continuum, and BD.

The Hamiltonian of continuum and atomistic domains are weighted by a scaling factor to avoid double counting of the Hamiltonian in the BD and to provide a gradual transition from the atomistic model to the continuum model.

A relaxed version of the BDM [33] has been developed to overcome the shortcoming of the original BDM in modeling composite lattice structures. Zhang et al. [14,15] used the BDM method to model cracks and defects in graphene and carbon nanotubes. The BDM has been used in coupled quantum mechanics, MD, and continuum mechanics simulations for investigating fracture properties of graphene sheets containing defects at zero temperature [16]. To more effectively model cracks and dislocations, the BDM has been combined with the extended FE method [17–19].

Although at zero temperature, a number of materials science problems involving both nonlinear and long-range deformation fields have been successfully simulated by the multiscale methods [14–19,34–40], multiscale simulations at finite temperature are more challenging. At finite temperature, a successful multiscale method should render atomistic and continuum models thermally compatible, because unlike MD models, continuum models divide the energy into mechanical and thermal components and the system is described by two time-dependent fields, the displacement and the temperature, which are governed by continuum equations of motion and heat equation. To perform finite-temperature simulations, extending the QM [41–43], the CGMD method [8], and the BSM [44] have been made. Recently, Mathew et al. [45] developed a coupled atomistic and continuum models at finite temperature but only applied to one-dimensional problems. Noting the above-mentioned advantages of the BDM, its extension to finite temperature is naturally of interest, and the BDM has been used in some finite-temperature multiscale simulations [12]. However, Anciaux et al. [20] recently analyzed the performance of the BDM at finite temperature, and revealed an artificial cooling effect on the coupled atoms, which leads to the emergence of a strong temperature gradient in the BD. Furthermore, application of thermostats to rectify the cooling effect in the original BDM formulation is unstable. This is because the BDM coupling technique damps too strongly the high-frequency atomic vibrations in the BD. Therefore, rectifying this artifact with an improved BDM is the focus of this paper.

Trying to overcome this problem, Anciaux et al. [20] separated the BD into two sub-zones as shown in Fig. 2. The FE displacements are constrained to match the MD solution in the first zone while the MD displacements are interpolated from the FE displacements in the second zone. Thermostatting is done in the first zone without any instability because in this zone atomic motion is not constrained to FE displacements. Although their technique rectifies the cooling effect, it has two disadvantages in comparison to the original BDM: (1) there is no treatment to remove spurious wave reflections across the coupling interface because Anciaux's method enforces direct constraints between atomic motion and FE displacements; and (2) their method does not employ scaling of the atomistic and continuum energies in the BD so that the transition from the atomistic model to the continuum model is not gradual.

In this paper, an improved BDM is proposed to rectify the cooling effect while using the conventional BDM algorithm to scale MD and FE energies in the BD for a smooth transition as well as damping out spurious wave reflections. In the proposed
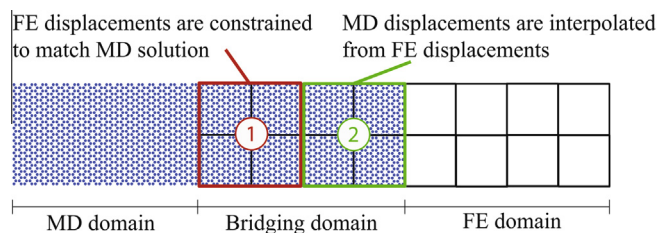

Fig. 2. Separated BD proposed by Anciaux et al. [20].

three-layer-mesh BDM (TBDM), atomic motion in the BD is partitioned into (1) thermal vibrations constituting thermal energy, and (2) mechanical waves contributing to mechanical energy. This partitioning is consistent with the continuum representations and accordingly, each part can be separately coupled with the continuum model. In the TBDM, temperature stability in the BD is achieved by constraining only the mechanical part of atomic motion to the FE displacements, i.e. thermal vibrations are excluded from the mechanical coupling between MD and FE. Unconstrained thermal vibrations are thermostatted using local thermostats in the BD. By using this algorithm, Lagrange multipliers in the TBDM formulation do not damp out thermal vibrations anymore, so that the source of cooling effect is eliminated.

Another useful feature of the proposed TBDM is that discrimination between thermal vibrations and mechanical deformations is independent of the continuum FE mesh. Although using the conventional BDM algorithm, atomic motion can also be decomposed into two parts: coarse part (resolved by the FE mesh) and fine part (not resolved by the FE mesh) [25], this decomposition is not the best means to discriminate between thermal and mechanical waves since it is a mesh-dependent definition. In this paper, we propose to use a mesh-independent physics-based discrimination between thermal and mechanical waves to define and introduce a meso mesh, which is independent of the FE mesh. Thermal vibrations are instant dynamic atomic displacements about "mean" atomic positions and mechanical deformations are net displacements of mean atomic positions. Thus, mechanical waves have much less kinetic energy in comparison with thermal vibrations. This physical concept is used in the TBDM to discriminate between thermal vibrations and mechanical waves. The "low-frequency" waves, whose kinetic energies have negligible effects on temperature, are considered as mechanical waves. The appropriate meso-mesh size, which is independent of the FE-mesh size, should be determined accordingly. This is achieved by preliminary numerical simulations, as presented in Section 4.3.

The TBDM employs a new three-layer mesh structure in the BD, consisting of coarse (FE), meso and fine (MD) meshes as shown in Fig. 3. It enables decomposition of total atomic motion into three parts of coarse, meso, and fine scales, so that the coarse and meso parts (i.e. mechanical deformation) are constrained to the FE displacements using the Lagrange multipliers technique similar to the conventional BDM, and the fine part is thermostatted within the BD using Langevin dynamics. Actually, using a three-layer mesh, we propose to decompose total atomic motion in the BD into: (1) thermal vibrations (fine part), (2) the mechanical waves that can be resolved by the continuum model (coarse part), and (3) the mechanical waves that cannot be resolved by the continuum model (meso part). The meso part is damped out using the absorbing boundary condition in the BDM formulation, as presented in [25], to suppress spurious wave reflection at the interface of atomistic and continuum models.

Generally, the choice for the coarse scale in the proposed BDM is to have large enough finite elements, so that the atoms inside each element in the BD can be considered as an appropriate ensemble to be thermostatted. In other words, the new mesh structure with an additional layer of meso-mesh allows one to use larger finite elements in the continuum domain than the conventional BDM, without any adverse effect on the determination of thermal vibrations. In summary, the FE-mesh size should be selected so that the FE mesh can (1) accurately model the mechanical waves which travel through the continuum domain and are transferred to the MD domain during the multiscale simulation, (2) provide realistic boundary conditions for the MD model in terms of stiffness, (3) accurately model the desired continuum heat-transfer event, and (4) be large enough to be considered as appropriate ensembles for local thermostats in the BD.

This new architecture of three-layer-mesh BD effectively mitigates the temperature cooling effect encountered by the conventional BDM as well as suppresses the spurious mechanical wave reflection using the Lagrange multipliers and the damping boundary condition [25]. Also, since the conventional BDM with energy scaling factors is used for coupling the coarse and meso parts of atomic motion and the FE displacements, a gradual transition between the atomistic and continuum models is provided.
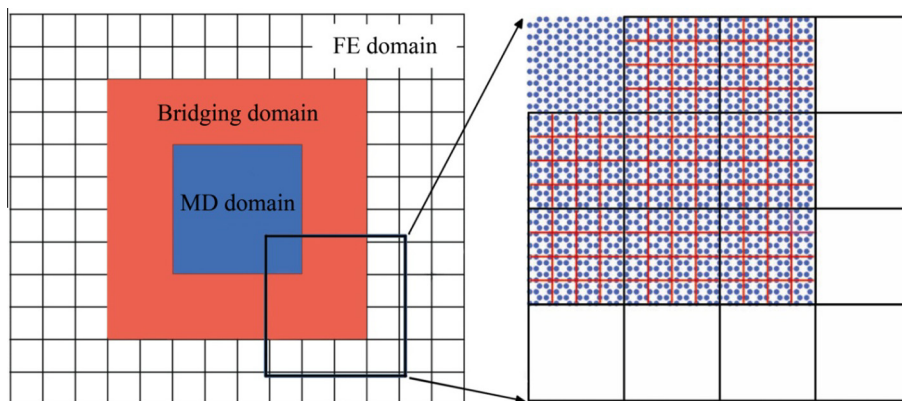

Fig. 3. FE mesh (black), meso mesh (red), and atomistic model (blue) in the three-layer-mesh BD. (For interpretation of the references to color in this figure legend, the reader is referred to the web version of this article.)

This paper aims to present the basic formulation of the TBDM at finite temperature. The robustness and accuracy of the proposed multiscale method at finite temperature are verified by some numerical simulations. We will present application of the TBDM in real-material simulation of graphene sheets using a realistic interatomic potential, the adaptive intermolecular reactive bond order (AIREBO) potential [46], in due course.

The outline of this paper is as follows: in Section 2, we briefly review some basic formulations of the BDM. Section 3 is dedicated to the formulations of the new three-layer-mesh BDM for finite-temperature simulations. Section 4 presents the numerical examples, followed by some conclusions made in Section 5.

2. Bridging domain method

Following the use of Lagrange multipliers for compatibility enforcement between atomistic and continuum displacement in the BD, the BDM divides the total Hamiltonian into three parts: atomistic Hamiltonian, continuum Hamiltonian, and the Hamiltonian associated with the Lagrange multipliers. The Hamiltonian of continuum and atomistic domains are weighted by a scaling factor to avoid double counting of Hamiltonian in the BD. The atomistic (continuum) energy is dominant near the purely atomistic (continuum) domain. This strategy provides a gradual transition from the atomistic model to the continuum model, and alleviates the error that arises from dropping the atomistic energies from far-field atoms.

$$H = H^C + H^A + G \tag{1}$$

where H^C is the continuum domain Hamiltonian, H^A is the Hamiltonian from the atomistic domain, and G is the Hamiltonian associated with the Lagrange multipliers that impose displacement compatibility of the atomistic and continuum domains at the BD.

The atomistic and continuum Hamiltonians are given by

$$H^A = \sum_{\alpha \in \mathcal{M}} \left(\vartheta_\alpha \frac{p^A_{i\alpha} p^A_{i\alpha}}{2m^A_\alpha} + \sum_{\beta \in \mathcal{M} > \alpha} \vartheta_{\alpha\beta} V_{\alpha\beta} \right) \tag{2}$$

and

$$H^C = \sum_{I,J \in \mathcal{S}} \left(\int_{\Omega^C_0} (1 - \vartheta) \frac{p^C_{iI} p^C_{iJ} N_I N_J}{2\rho_0} d\Omega + \int_{\Omega^C_0} (1 - \vartheta) W^C(\mathbf{F}) d\Omega \right) \tag{3}$$

in which $\mathcal{M}$ and $\mathcal{S}$ are the sets of all atoms and all FE nodes respectively, $\vartheta = \vartheta(\mathbf{X})$ is the energy scaling function, $\vartheta_\alpha = \vartheta(\mathbf{X}_\alpha)$ and $\vartheta_{\alpha\beta} = (\vartheta_\alpha + \vartheta_\beta)/2$, $p^A_{i\alpha}$ is the ith component of the linear momentum of atom α, p^C_{iI} is the ith component of the linear momentum of node I, $N_I(\mathbf{X})$ is the FE shape function of node I, m^A_α is the mass of atom α, ρ_0 is the initial density of the continuum domain, $V_{\alpha\beta}$ is the interatomic potential associated with the bond between atoms α and β, $\mathbf{F} = \partial\mathbf{x}/\partial\mathbf{X}$ is the deformation gradient, and W^C is the FE strain energy density at finite temperature, which can be obtained from the atomistic model using the temperature-related Cauchy–Born rule [47,48] detailed in Section 4.1 below.

Throughout this paper, $\mathbf{X}$ denotes the material (Lagrangian or initial) coordinates and $\mathbf{x}$ denotes the spatial (Eulerian or current) coordinates. Also, we use the Einstein notation: repeated indices indicate summation for the lower case subscripts denoting the components of the material coordinates. It should be noted that although Eq. (2) uses pair-wise interatomic potentials for convenience, the BDM applies also to many-body potentials. Using the notation, introduced in Fig. 1, the linear energy scaling function, which is usually used in BDM simulations, is defined as

$$\vartheta(\mathbf{X}) = \begin{cases} 0, & \text{in } \left(\Omega^C_0 - \Omega^B_0\right) \text{ and on } \Gamma^C \\ 1 - \frac{r^B}{L^B} \in [0, 1], & \text{in } \Omega^B_0 \\ 1, & \text{in } \left(\Omega^A_0 - \Omega^B_0\right) \text{ and on } \Gamma^A \end{cases} \tag{4}$$

where $\vartheta(\mathbf{X})$ is the weight function, $L^{|B}$ is the thickness of the BD and $r^{|B}$ is the distance between point $\mathbf{X}$ inside the BD and the atomistic edge Γ^A.

Guidault and Belytschko discussed the choice of the weight function in the BDM [31,32]. They showed that both continuous and discontinuous weight functions can be used with the H^1 coupling whereas continuous weight functions are required to be used with the L^2 coupling. Their investigation also showed that L^2 coupling produces less error in comparison to the H^1 coupling. The effects of different choices for the weight function are also studied in the framework of other similar methods to the BDM, and the conclusions are also applicable to the BDM. The effects of using constant, linear, and cubic weight functions in the Arlequin method were studied in [49], which revealed that linear and cubic weight functions are beneficial over constant weight functions. Recently, Luskin et al. further investigated the choice of the weight function in the framework of the energy-based blended quasicontinuum method [50–52]. They showed that the linear weight function gives a singularity at the boundary of the bridging region that reduces the order of the approximation, and the order of approximation can be improved by a smoother weight function.

In the BDM, the compatibility between atomistic and continuum models in the BD can be imposed stringently by associating one Lagrange multiplier with each degree of freedom of each atom in the BD, or it can be applied weakly by approximating the Lagrange multipliers from the finite element mesh i.e. one Lagrange multiplier is associated with each degree of freedom of each FE-node in the BD [12,17]. The latter algorithm is used in this paper to develop the three-layer-mesh BDM since it has lower computational cost in comparison with the first algorithm and it is shown that by using damping boundary conditions in the BDM formulation, the weak enforcement of the compatibility is as effective as the strict enforcement [25]. The Hamiltonian associated with the Lagrange multipliers is given by

$$G = \sum_{I \in \mathcal{S}^{B}} \lambda_{iI} \left[\sum_{\alpha \in \mathcal{M}^{B}} N_{I\alpha} \left(\sum_{J \in \mathcal{S}^{B}} N_{J\alpha} u_{iJ} - d_{i\alpha} \right) \right], \tag{5}$$

where $\mathcal{M}^{B}$ and $\mathcal{S}^{B}$ are the sets of the atoms and FE nodes in the BD respectively, λ_{iI} is the Lagrange multiplier associated with the ith degree of freedom of node I. $N_{I\alpha} = N_{I}(\mathbf{X}_{\alpha})$ is the FE shape function of node I at the position of atom α, u_{iJ} and $d_{i\alpha}$ are the ith component of the displacement of node J and atom α respectively.

Total Lagrangian of the system is obtained from Legendre transformation of the total Hamiltonian. Using Lagrange's equations, the equations of motion are obtained from the total Lagrangian as [26]

$$M_{\alpha}^{A}\ddot{d}_{i\alpha} + \left(f_{i\alpha}^{\text{int}}\right)^{A} + \left(f_{i\alpha}^{G}\right)^{A} = 0, \quad \forall \alpha \in \mathcal{M} \tag{6a}$$

$$M_{I}^{C}\ddot{u}_{iI} + \left(f_{iI}^{\text{int}}\right)^{C} + \left(f_{iI}^{G}\right)^{C} = 0, \quad \forall I \in \mathcal{S} \tag{6b}$$

where

$$M_{\alpha}^{A} = \vartheta_{\alpha}m_{\alpha}^{A} \tag{7a}$$

$$M_{I}^{C} = \sum_{J \in \mathcal{S}} \int_{\Omega_{0}^{C}} (1 - \vartheta)\rho_{0}N_{I}N_{J}d\Omega \tag{7b}$$

$$\left(f_{i\alpha}^{\text{int}}\right)^{A} = \vartheta_{\alpha\beta}\frac{\partial V}{\partial d_{i\alpha}} = \vartheta_{\alpha\beta}\sum_{\beta \in \mathcal{M}}\frac{\partial V_{\alpha\beta}}{\partial d_{i\alpha}} \tag{7c}$$

$$\left(f_{iI}^{\text{int}}\right)^{C} = \int_{\Omega_{0}^{C}} (1 - \vartheta)\frac{\partial W^{C}}{\partial u_{iI}}d\Omega = \int_{\Omega_{0}^{C}} (1 - \vartheta)\frac{\partial N_{I}}{\partial \mathbf{X}_{j}}P_{ji}d\Omega \tag{7d}$$

$$\left(f_{i\alpha}^{G}\right)^{A} = \frac{\partial G}{\partial d_{i\alpha}} = -\sum_{I \in \mathcal{S}^{B}}N_{I\alpha}\lambda_{iI} \tag{7e}$$

$$\left(f_{i\alpha}^{G}\right)^{C} = \frac{\partial G}{\partial u_{iI}} = \sum_{\alpha \in \mathcal{M}^{B}}\sum_{I \in \mathcal{S}^{B}}N_{J\alpha}N_{I\alpha}\lambda_{iJ} \tag{7f}$$

in which P_{ji} are the components of the first Piola–Kirchhoff stress tensor, and the Lagrange multipliers are governed by the following equations

$$\frac{\partial H}{\partial \lambda_{iI}} = \sum_{\alpha \in \mathcal{M}^{B}}\sum_{J \in \mathcal{S}^{B}}N_{I\alpha}N_{J\alpha}u_{iI} - \sum_{\alpha \in \mathcal{M}^{B}}N_{I\alpha}\,d_{i\alpha} = 0, \quad \forall I \in \mathcal{S}^{B} \tag{8}$$

Since total Lagrangian description of the momentum equation is used in nonlinear finite element formulations in the conventional BDM, consistently, we use total Lagrangian description of the energy equation to obtain changes of the temperature in the continuum model during the simulation. The energy equation can be written as

$$\mathbf{C}_{T} : \dot{\mathbf{F}} + C_{\mathbf{F}}\dot{T} + \nabla_{\mathbf{X}} \cdot (J\mathbf{F}^{-1}\mathbf{K}\mathbf{F}^{-T}\nabla_{\mathbf{X}}T) = 0 \tag{9}$$

in which $\dot{\mathbf{F}}$ is the rate of the deformation gradient, $J = \det(\mathbf{F})$ is the Jacobian, and $\mathbf{C}_{T}$ and $C_{\mathbf{F}}$ are the specific heat capacities at constant temperature and constant strain, respectively. Our heat-transfer simulations in this paper does not include internal heat source and mechanical strain, therefore, we ignore terms $\rho_{0}z$ and $\mathbf{C}_{T} : \dot{\mathbf{F}}$ in Eq. (9) in the rest of this paper.

To have a seamlessly coupled atomistic–continuum model, the continuum material constants should be consistent with the atomistic model. For this purpose, we use the temperature-related Cauchy–Born rule [47,48] to obtain the continuum constitutive model. Also, thermal conductivity and specific heat capacity at constant strain are calibrated in preliminary fully atomistic simulations. Details of determining continuum material constants are presented in Sections 4.1 and 4.2.

3. Three-layer-mesh bridging domain method (TBDM)

TBDM is designed to overcome the artificial cooling effect, recently observed on the coupled atoms in the conventional BDM simulations by Anciaux et al. [20]. The source of this cooling effect is that the BDM coupling technique damps too strongly the high-frequency atomic vibrations in the BD. To avoid damping the thermal vibrations in the BD within the BDM formulation, we propose a new decomposition of the atomic motion in the BD by employing a three-layer mesh structure in the BD. The three-layer mesh (Fig. 3) consists of coarse, meso and fine meshes, which enables decomposition of total atomic motion into three parts of coarse, meso, and fine scales. The coarse and meso parts are constrained to the FE displacements using the Lagrange multipliers technique, and the fine part (thermal vibration) is thermostatted within the BD using Langevin dynamics. Below, we first present the proposed decomposition scheme of atomic motion in the TBDM; then, we explain how to employ the conventional BDM formulation with damping to quench the coarse and meso parts to the continuum model as well as how to thermostat thermal vibrations.

3.1. Decomposition of atomic motion in the bridging domain

We propose to decompose atomic motion in the BD into three parts:

$$d_{i\alpha} = (d_{i\alpha})^{\text{coarse}} + (d_{i\alpha})^{\text{meso}} + (d_{i\alpha})^{\text{fine}}, \quad \forall \alpha \in \mathcal{M}^{\text{B}} \tag{10}$$

where $d_{i\alpha}$ is total displacement of atom α in the ith direction, $(d_{i\alpha})^{\text{coarse}}$, $(d_{i\alpha})^{\text{meso}}$ and $(d_{i\alpha})^{\text{fine}}$ are its coarse, meso and fine components, respectively. The continuum displacement field constitutes the coarse-scale part of the displacement field, and is approximated by the standard FE interpolation at atomic positions

$$(d_{i\alpha})^{\text{coarse}} = u_i(\mathbf{X}_\alpha) = \sum_I N_{I\alpha} u_{iI} \tag{11}$$

in which u_{iI} is the displacement of node I in the ith direction, and $N_{I\alpha}$ is the FE shape function associated with node I at the position of atom α. The meso-scale part of atomic displacements is obtained by subtracting the coarse part from the displacements which can be resolved by the meso mesh (i.e. the mechanical part of atomic motion $(d_{i\alpha})^{\text{mech}}$):

$$(d_{i\alpha})^{\text{meso}} = (d_{i\alpha})^{\text{mech}} - (d_{i\alpha})^{\text{coarse}}, \quad \forall \alpha \in \mathcal{M}^e \tag{12}$$

The mechanical part of atomic motion is obtained by interpolating the meso-mesh displacements over each finite element e in the BD:

$$(d_{i\alpha})^{\text{mech}} = u_i^{\text{meso}}(\mathbf{X}_\alpha) = \sum_{p \in {}^e\mathcal{S}^{\text{meso}}} N_{p\alpha}^{\text{meso}} u_{ip}^{\text{meso}}, \quad \forall \alpha \in \mathcal{M}^e \tag{13}$$

where e is the finite element containing atom α, ${}^e\mathcal{S}^{\text{meso}}$ is the set of all meso-mesh nodes whose supports intersect with finite element e, $\mathcal{M}^e$ is the set of all atoms in finite element e, $N_{p\alpha}^{\text{meso}}$ is the shape function associated with mesomesh node p at the position of atom α, and u_{ip}^{meso} is the ith component of the displacement associated with node p of the mesomesh, which is obtained by the least-square fit of the mesomesh displacement field to the atomic displacement in finite element e:

$$\begin{aligned} \min(\Delta) &= \min\left[\sum_{\alpha \in \mathcal{M}^e} \left(u_i^{\text{meso}}(\mathbf{X}_\alpha) - d_{i\alpha}\right)\left(u_i^{\text{meso}}(\mathbf{X}_\alpha) - d_{i\alpha}\right) \right] \\ &= \min\left[\sum_{\alpha \in \mathcal{M}^e} \left(\sum_{p \in {}^e\mathcal{S}^{\text{meso}}} N_{p\alpha}^{\text{meso}} u_i^{\text{meso}} - d_{i\alpha} \right)\left(\sum_{p \in {}^e\mathcal{S}^{\text{meso}}} N_{p\alpha}^{\text{meso}} u_i^{\text{meso}} - d_{i\alpha} \right) \right] \end{aligned} \tag{14}$$

which leads to

$$\frac{\partial \Delta}{\partial u_{iq}^{\text{meso}}} = \sum_{\alpha \in \mathcal{M}^e} \left[N_{q\alpha}^{\text{meso}} \left(\sum_{p \in {}^e\mathcal{S}^{\text{meso}}} N_{p\alpha}^{\text{meso}} u_{ip}^{\text{meso}} - d_{i\alpha} \right) \right] = 0 \tag{15}$$

Eq. (15) can be solved for the meso-mesh nodal displacements as

$$\mathbf{u}_i^{\text{meso}} = \left[{}^e\mathbf{N}^{\text{meso}} ({}^e\mathbf{N}^{\text{meso}})^{\text{T}} \right]^{-1} {}^e\mathbf{N}^{\text{meso}} \mathbf{d}_i \tag{16}$$

where $\mathbf{u}_i^{\text{meso}} = \{u_{ip}^{\text{meso}}, \forall p \in {}^e\mathcal{S}^{\text{meso}}\}$ is the vector of ith component of nodal displacements of the meso-mesh nodes whose supports intersect with finite element e, $\mathbf{d}_i = \{d_{i\alpha}, \forall \alpha \in \mathcal{M}^e\}$ is the vector of ith component of the displacements of all atoms in finite element e, and ${}^e N_{p\alpha}^{\text{meso}} = N_p^{\text{meso}}(\mathbf{X}_\alpha)$ is the meso-mesh interpolation matrix associated with finite element e. Substituting Eq. (16) into Eq. (13) gives

$$\mathbf{d}_i^{\text{mech}} = \mathbf{P}^e \mathbf{d}_i \tag{17}$$

in which $\mathbf{P}^{e}$ is the projection operator associated with finite element e, which is obtained as

$$\mathbf{P}^{e} = \left({}^{e}\mathbf{N}^{meso}\right)^{T}\left[{}^{e}\mathbf{N}^{meso}\left({}^{e}\mathbf{N}^{meso}\right)^{T}\right]^{-1}{}^{e}\mathbf{N}^{meso}. \tag{18}$$

Finally, the fine-scale part of atomic displacements is calculated by subtracting the mechanical part from the total displacements

$$\mathbf{d}_{i}^{fine} = \mathbf{d}_{i} - \mathbf{d}_{i}^{mech} = (\mathbf{I} - \mathbf{P}^{e})\mathbf{d}_{i} \tag{19}$$

in which $\mathbf{I}$ is the identity matrix.

Strictly, we want to retain the efficiency of the BDM in our new TBDM for finite-temperature simulations. The proposed decomposition is computationally inexpensive because (1) projection operator $\mathbf{P}^{e}$ is computed once based on the initial configuration before simulation loop starts, and used for all time steps, (2) $\mathbf{P}^{e}$ is local in the sense that its domain and codomain are confined to those atoms inside a single finite element e, and (3) the meso-mesh topology and data structure are not needed after the computation of $\mathbf{P}^{e}$, and they may be removed from the computer memory before starting the main loop over time steps.

3.2. The TBDM algorithm

In this section, at first we explain how each of the MD and FE models provides required temperature boundary conditions for each other in the BD and then, we present the proposed algorithm of the TBDM in the BD, followed by the associated formulations.

In the TBDM, the coarse and meso parts of atomic motion in the BD are constrained to the FE displacements using the Lagrange multipliers technique, and the fine part (thermal vibration) is thermostatted within the BD. Large enough finite elements are used, so that the atoms inside each element in the BD can be considered as an appropriate ensemble to be thermostatted. The FE solution provides the target temperature for thermostatting thermal vibrations of the atomistic model within each FE element in the BD (Fig. 4):

$$^{e}T^{target} = \frac{1}{n}\sum_{I \in \mathcal{S}^{e}}T_{I}. \tag{20}$$

where n is the number of the nodes of each FE element, $\mathcal{S}^{e}$ is the set of all FE nodes of element e, and T_{I} is the nodal temperature at node I.

On the other hand, temperature boundary conditions for the FE model at the ghost nodes (Fig. 4) are determined by the calculated temperatures from the atomistic model. In the ensemble around ghost FE node I, which is assumed to be canonical, temperature is expressed in terms of an average of the kinetic energy of the atoms inside the ensemble:

$$\overline{T}_{I} = \frac{2}{dk_{B}n_{I}^{a}}\sum_{\alpha \in \mathcal{E}^{I}}\frac{1}{2}m_{\alpha}^{A}v_{\alpha}^{2} \tag{21}$$
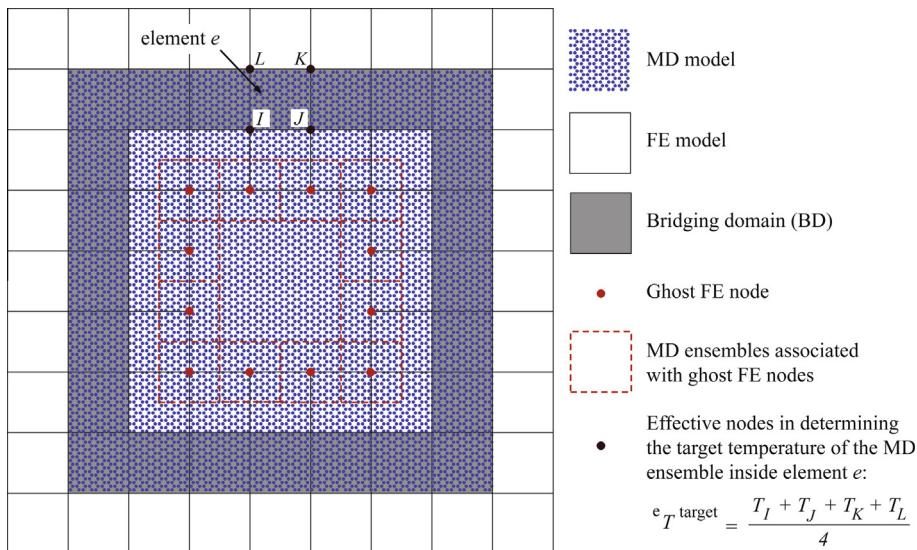

Fig. 4. The atoms inside each element in the BD are thermostatted to reach the target temperature of that element. Temperature boundary conditions for the FE model at the ghost nodes are determined by the calculated temperatures from the atomistic model.

where d is the dimension of the space, k_B is the Boltzmann constant, n_I^a is the number of the atoms in the ensemble associated with ghost FE node I, $\mathcal{E}^I$ is the set of all atoms inside the ensemble, m_α and v_α are the mass and the velocity of atom α, respectively. During the simulation, the ghost FE nodes move with the atoms near them so we do not need to solve the momentum equation to update their positions.

The Verlet algorithm is used for time integration of the MD equations of motion and the FE momentum equation, and the forward Euler algorithm is used in time integration of the FE energy equation (Eq. (9)). In the following, we describe the details of the time-integration scheme, used in the TBDM, for integration of the equations of motion.

Based on the Verlet algorithm, before time step $n + 1$, $\mathbf{d}^n$, $\dot{\mathbf{d}}^{n-1}$, $\ddot{\mathbf{d}}^{n-1}$, $\mathbf{u}^n$, $\dot{\mathbf{u}}^{n-1}$, and $\ddot{\mathbf{u}}^{n-1}$ are known. $\mathbf{d}^n$, $\dot{\mathbf{d}}^{n-1}$, $\ddot{\mathbf{d}}^{n-1}$ are the vectors of all atomic displacements, velocities, and accelerations, respectively, and $\mathbf{u}^n$, $\dot{\mathbf{u}}^{n-1}$, $\ddot{\mathbf{u}}^{n-1}$ are the vectors of all FE nodal displacements, velocities, and accelerations, respectively. Since the Lagrange multipliers (λ^n) are unknown before time step $n + 1$, a predictor–corrector scheme is adopted in the BDM. At first, displacements are updated in the predictor step without considering the Lagrange multipliers then, the Lagrange multipliers are computed based on these predicted values and finally, displacements and velocities are modified in the corrector step. The steps of the TBDM algorithm at time step $n + 1$ are summarized in Fig. 5.

At time step $n + 1$, using Eqs. ((6a,b) and (7a-d)) predicted atoms accelerations $(\ddot{\mathbf{d}}^n)^*$ and predicted FE nodal accelerations $(\ddot{\mathbf{u}}^n)^*$ are calculated based on the interatomic potentials and the continuum constitutive model, respectively, without considering Lagrange multipliers.

$$\left(\ddot{d}_{i\alpha}^n\right)^* = -\frac{\left(\left(f_{i\alpha}^{\text{int}}\right)^A\right)^n}{M_\alpha^A} \tag{22a}$$
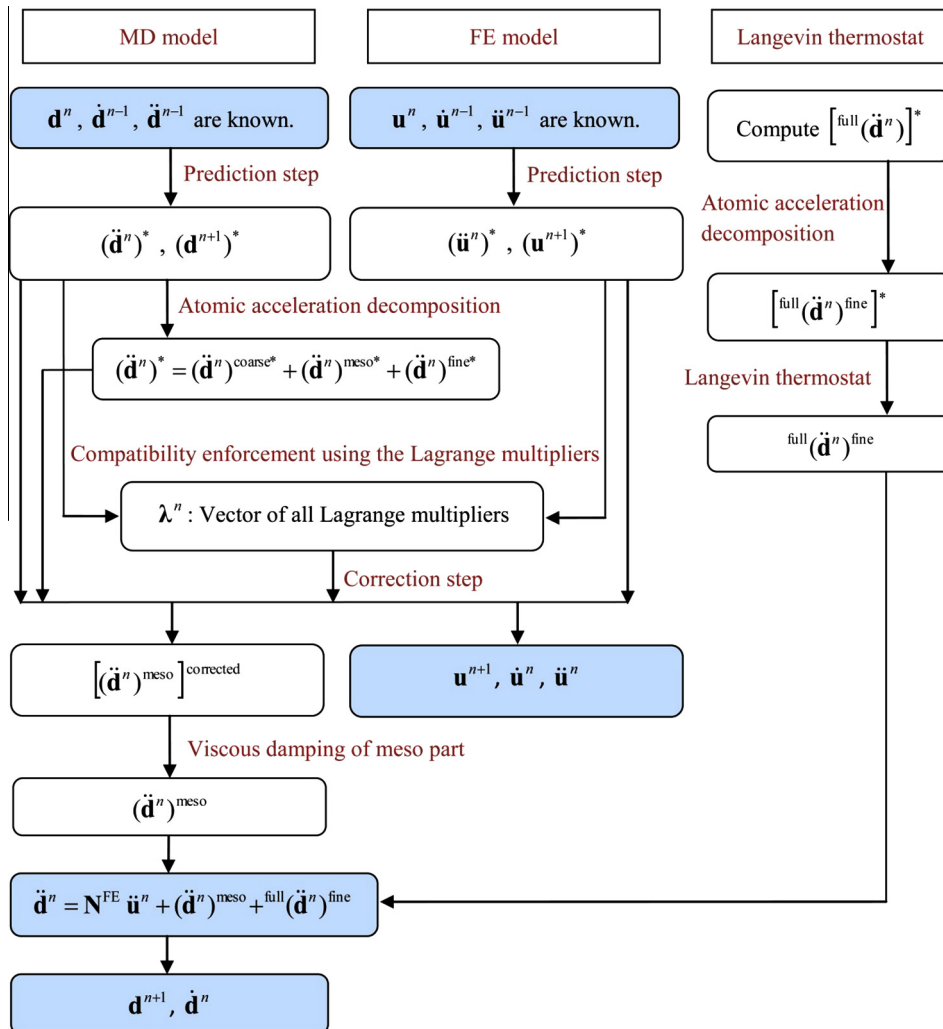

Fig. 5. Steps of the TBDM algorithm at time step $n + 1$ using the predictor–corrector time integration for the equations of motion.

$$\left(\ddot{u}_{iI}^n\right)^* = -\frac{\left(\left(f_{iI}^{\text{int}}\right)^C\right)^n}{M_I^C}. \tag{22b}$$

The Verlet algorithm, which uses the central difference approximation, is adopted for time integration in the BDM (e.g. [26]). By substituting Eq. (7e,f) into the equations of motion (6a,b) and using the Verlet time-integration formulation, MD and FE displacements can be updated as

$$d_{i\alpha}^{n+1} = \left(d_{i\alpha}^{n+1}\right)^* + \frac{(\Delta t)^2}{M_\alpha^A} \sum_{I \in \mathcal{S}^B} N_{I\alpha} \lambda_{iI}^n \tag{23a}$$

$$u_{iI}^{n+1} = \left(u_{iI}^{n+1}\right)^* - \frac{(\Delta t)^2}{M_I^C} \sum_{\alpha \in \mathcal{M}^B} \sum_{J \in \mathcal{S}^B} N_{I\alpha} N_{J\alpha} \lambda_{iJ}^n \tag{23b}$$

in which Δt is the time step and the predicted displacements are

$$\left(d_{i\alpha}^{n+1}\right)^* = \left(\ddot{d}_{i\alpha}^n\right)^* (\Delta t)^2 + 2d_{i\alpha}^n - d_{i\alpha}^{n-1} \tag{24a}$$

$$\left(u_{iI}^{n+1}\right)^* = \left(\ddot{u}_{iI}^n\right)^* (\Delta t)^2 + 2u_{iI}^n - u_{iI}^{n-1}. \tag{24b}$$

By substituting Eq. (23) into Eq. (8), the Lagrange multipliers can be obtained as

$$\sum_{J \in \mathcal{S}^B} A_{IJ} \lambda_{iJ}^n = \sum_{\alpha \in \mathcal{M}^B} \sum_{K \in \mathcal{S}^B} N_{I\alpha} N_{K\alpha} \left(u_{iK}^{n+1}\right)^* - \sum_{\alpha \in \mathcal{M}^B} N_{I\alpha} \left(d_{i\alpha}^{n+1}\right)^* \tag{25}$$

where

$$A_{IJ} = \sum_{\alpha \in \mathcal{M}^B} \sum_{K \in \mathcal{S}^B} \sum_{\beta \in \mathcal{M}^B} \frac{(\Delta t)^2}{M_K^C} N_{I\alpha} N_{J\beta} N_{K\alpha} N_{K\beta} - \sum_{\alpha \in \mathcal{M}^B} \frac{(\Delta t)^2}{M_\alpha^A} N_{I\alpha} N_{J\alpha} \tag{26}$$

One important step in the BDM is the diagonalization of the constraint matrix as

$$A_I = \sum_{J \in \mathcal{S}^B} A_{IJ} \tag{27}$$

which is essential for eliminating spurious wave reflection [26].

In the TBDM, the MD/FE displacement compatibility should be enforced between the FE displacements field and the coarse and meso parts of atoms displacements. This is done in Eq. (25) where we enforce the compatibility condition between the FE displacements and total displacements of the atoms. This strategy alleviates the need for the decomposition of atomic displacements in this part of the TBDM algorithm, which has a positive effect on the TBDM efficiency. Numerical simulations showed that high-frequency atomic displacements do not significantly affect the Lagrange multipliers in the TBDM algorithm.

In the predictor–corrector time-integration algorithm, at first, predicted displacements are evaluated at time step $n + 1$ using Eq. (24), and then the Lagrange multipliers are computed using Eq. (25). Finally, the corrected FE nodal accelerations, velocities and displacements are obtained, respectively, as

$$\ddot{u}_{iI}^n = \left(\ddot{u}_{iI}^n\right)^* - \frac{1}{M_I^C} \sum_{\alpha \in \mathcal{M}^B} \sum_{J \in \mathcal{S}^B} N_{I\alpha} N_{J\alpha} \lambda_{iJ}^n \tag{28a}$$

$$\dot{u}_{iI}^n = \dot{u}_{iI}^{n-1} + \left(\ddot{u}_{iI}^{n-1} + \ddot{u}_{iI}^{n-1}\right) \frac{\Delta t}{2}. \tag{28b}$$

$$u_{iI}^{n+1} = \ddot{u}_{iI}^n (\Delta t)^2 + 2u_{iI}^n - u_{iI}^{n-1} \tag{28c}$$

The computed Lagrange multipliers also affect the coarse and meso parts (i.e. the mechanical part) of atomic motion. We derive the corrected meso part since the viscous damping [25] should be applied on this part to damp out the spurious mechanical reflection. Using the decomposition algorithm (presented in Section 3.1), predicted atomic accelerations (Eq. (22a)) can be decomposed as

$$\left(\ddot{d}_{i\alpha}^n\right)^* = \left[\left(\ddot{d}_{i\alpha}^n\right)^{\text{mech}}\right]^* + \left[\left(\ddot{d}_{i\alpha}^n\right)^{\text{fine}}\right]^*, \quad \forall \alpha \in \mathcal{M}^B \tag{29}$$

As mentioned before, the Lagrange multipliers affect the mechanical part of atomic motion so noting Eqs. ((6a), (7e), (22a)), the corrected coarse and meso parts can be written as

$$\left[\left(\ddot{d}_{i\alpha}^n\right)^{\text{mech}}\right]^{\text{corrected}} = \left[\left(\ddot{d}_{i\alpha}^n\right)^{\text{mech}}\right]^* + \frac{1}{M_\alpha^{\text{A}}}\sum_{I\in\mathcal{S}^{\text{B}}}N_{I\alpha}\lambda_{iI}^n \tag{30}$$

By substituting the second time-derivatives of Eqs. (11) and (12) into Eq. (30), the corrected meso part is

$$\left[\left(\ddot{d}_{i\alpha}^n\right)^{\text{meso}}\right]^{\text{corrected}} = \left(\left[\left(\ddot{d}_{i\alpha}^n\right)^{\text{mech}}\right]^* + \frac{1}{M_\alpha^{\text{A}}}\sum_{I\in\mathcal{S}^{\text{B}}}N_{I\alpha}\lambda_{iI}^n\right) - \sum_{I\in\mathcal{S}^{\text{B}}}N_{I\alpha}\ddot{u}_{iI}^n \tag{31}$$

which is the meso part of the atomic acceleration after applying the Lagrange multipliers but before applying the damping. To effectively damp out spurious reflections of the meso part displacements, which cannot be resolved by the FE mesh, a viscous damping term can be used

$$\left(\ddot{d}_{i\alpha}^n\right)^{\text{meso}} = \left[\left(\ddot{d}_{i\alpha}^n\right)^{\text{meso}}\right]^{\text{corrected}} - \xi_\alpha^{\text{meso}}\left(\dot{d}_{i\alpha}^n\right)^{\text{meso}} \tag{32}$$

where $(\dot{d}_{i\alpha}^n)^{\text{meso}}$ is obtained by solving the following Verlet time-integration equation

$$\left(\dot{d}_{i\alpha}^n\right)^{\text{meso}} = \left(\dot{d}_{i\alpha}^{n-1/2}\right)^{\text{meso}} + \frac{\Delta t}{2}\left(\ddot{d}_{i\alpha}^n\right)^{\text{meso}} = \left(\dot{d}_{i\alpha}^{n-1/2}\right)^{\text{meso}} + \frac{\Delta t}{2}\left\{\left[\left(\ddot{d}_{i\alpha}^n\right)^{\text{meso}}\right]^{\text{corrected}} - \xi_\alpha^{\text{meso}}\left(\dot{d}_{i\alpha}^n\right)^{\text{meso}}\right\} \tag{33}$$

as

$$\left(\dot{d}_{i\alpha}^n\right)^{\text{meso}} = \frac{\left(\dot{d}_{i\alpha}^{n-1/2}\right)^{\text{meso}} + \frac{\Delta t}{2}\left[\left(\ddot{d}_{i\alpha}^n\right)^{\text{meso}}\right]^{\text{corrected}}}{1 + \frac{\Delta t}{2}\xi_\alpha^{\text{meso}}} \tag{34}$$

in which $(\dot{d}_{i\alpha}^{n-1/2})^{\text{meso}}$ is obtained from $\dot{d}_{i\alpha}^{n-1/2}$ using the decomposition algorithm (presented in Section 3.1), and $\dot{d}_{i\alpha}^{n-1/2}$ is calculated using the Verlet algorithm as

$$\dot{d}_{i\alpha}^{n-1/2} = \dot{d}_{i\alpha}^{n-1} + \frac{\Delta t}{2}\ddot{d}_{i\alpha}^{n-1}. \tag{35}$$

By this point, the meso part (Eq. (32)) and the coarse part (Eqs. (28a) and (11)) of the atomic accelerations are updated at step n, the only remaining part is the fine (thermal) part, which is explained in the following.

To not disturb thermal vibrations of the atoms in the BD, full atomic accelerations $[^{\text{full}}(\ddot{d}_{i\alpha}^n)]^*$ are re-computed without considering the BDM energy scaling factor. Previously computed atomic accelerations in Eqs. (22a) and (7c), were scaled by the energy scaling factor. Similar computation should be repeated without considering the scaling factor for the atoms in the BD. To maintain the efficiency, in the actual implementation, we compute the interatomic forces once and then, store them twice: with and without the scaling factor.

Fine-scale part of the full atomic accelerations can be calculated using the second time-derivative of Eq. (19). To maintain target temperature for the MD model in the BD, the Langevin thermostat is used. Langevin dynamics is developed to account for omitted degrees of freedom in molecular systems by the use of stochastic differential equations [53]. Langevin dynamics also allows controlling the temperature in MD simulations. In the TBDM, the Langevin equation for the fine part of the atomic accelerations can be written as

$$^{\text{full}}\left(\ddot{d}_{i\alpha}^n\right)^{\text{fine}} = \left[^{\text{full}}\left(\ddot{d}_{i\alpha}^n\right)^{\text{fine}}\right]^* - \xi_\alpha^{\text{Lang}}\left(\dot{d}_{i\alpha}^n\right)^{\text{fine}} - R_i(t)\sqrt{\frac{2\xi_\alpha^{\text{Lang}}k_{\text{B}}T^{\text{target}}}{M_\alpha^{\text{A}}}} \tag{36}$$

in which ξ_α^{Lang} is the Langevin damping constant, k_{B} is the Boltzmann constant, and $\mathbf{R}(t)$ is a vector of delta-correlated stationary Gaussian variables with zero-mean, satisfying

$$\langle\mathbf{R}(t)\rangle = \mathbf{0} \tag{37a}$$

$$\langle\mathbf{R}(t)\otimes\mathbf{R}(t')\rangle = \mathbf{I}\delta(t - t') \tag{37b}$$

where $\otimes$ denotes the tensor product and $\delta(t - t')$ is the Dirac delta function.

In Eq. (36), $(\dot{d}_{i\alpha}^n)^{\text{fine}}$ is obtained by solving the following Verlet time-integration equation

$$\left(\dot{d}_{i\alpha}^n\right)^{\text{fine}} = \left(\dot{d}_{i\alpha}^{n-1/2}\right)^{\text{fine}} + \frac{\Delta t}{2}\left\{\left[^{\text{full}}\left(\ddot{d}_{i\alpha}^n\right)^{\text{fine}}\right]^* - \xi_\alpha^{\text{Lang}}\left(\dot{d}_{i\alpha}^n\right)^{\text{fine}} - R_i(t)\sqrt{\frac{2\xi_\alpha^{\text{Lang}}k_{\text{B}}T^{\text{target}}}{M_\alpha^{\text{A}}}}\right\} \tag{38}$$

as

$$\left(\dot{d}_{i\alpha}^n\right)^{\text{fine}} = \frac{\left(\dot{d}_{i\alpha}^{n-1/2}\right)^{\text{fine}} + \frac{\Delta t}{2}\left\{\left[^{\text{full}}\left(\ddot{d}_{i\alpha}^n\right)^{\text{fine}}\right]^* - \xi_\alpha^{\text{Lang}}\left(\dot{d}_{i\alpha}^n\right)^{\text{fine}} - R_i(t)\sqrt{\frac{2\xi_\alpha^{\text{Lang}}k_{\text{B}}T^{\text{target}}}{M_\alpha^{\text{A}}}}\right\}}{1 + \frac{\Delta t}{2}\xi_\alpha^{\text{Lang}}} \tag{39}$$

in which $(\dot{d}_{i\alpha}^{n-1/2})^{\text{fine}}$ is obtained from $\dot{d}_{i\alpha}^{n-1/2}$ using the decomposition algorithm, presented in Section 3.1, and $\dot{d}_{i\alpha}^{n-1/2}$ is already calculated in Eq. (35).

Finally, total atomic accelerations can be obtained as

$$\ddot{d}_{i\alpha}^n = \sum_{I \in \mathcal{S}^B} N_{I\alpha} \ddot{u}_{iI}^n + \left(\ddot{d}_{i\alpha}^n\right)^{\text{meso}} + {}^{\text{full}}\left(\ddot{d}_{i\alpha}^n\right)^{\text{fine}}, \quad \forall \alpha \in \mathcal{M}^B \tag{40}$$

where $\ddot{u}_{iI}^n$, $\left(\ddot{d}_{i\alpha}^n\right)^{\text{meso}}$, and ${}^{\text{full}}\left(\ddot{d}_{i\alpha}^n\right)^{\text{fine}}$ are calculated in Eqs. (28a), (32), and (36) respectively, and finally the atomic velocities and displacements are updated using the Verlet algorithm as

$$\dot{d}_{i\alpha}^n = \dot{d}_{i\alpha}^{n-1} + \left(\ddot{d}_{i\alpha}^{n-1} + \ddot{d}_{i\alpha}^n\right) \frac{\Delta t}{2} \tag{41a}$$

$$d_{i\alpha}^{n+1} = \ddot{d}_{i\alpha}^n (\Delta t)^2 + 2d_{i\alpha}^n - d_{i\alpha}^{n-1}. \tag{41b}$$

4. Numerical examples

To evaluate the performance of the proposed TBDM, we solve three numerical examples: (1) an equilibration example is simulated to demonstrate rectifying the cooling effects in the BD, (2) a heat transfer example is solved to show the effectiveness of the proposed thermal coupling algorithm, and (3) a wave propagation example at finite temperature is simulated to show that the TBDM can accurately transfer low-frequency waves between different models while damping out high-frequency mechanical waves, coming out from the MD zone.

In all numerical simulations, a triangular lattice, which corresponds to the [1 1 1] plane of an FCC crystal with lattice constant 0.3645 nm, is considered. The Lennard–Jones interatomic potential

$$V(r_{\alpha\beta}) = 4\varepsilon \left[\left(\frac{\sigma}{r_{\alpha\beta}}\right)^{12} - \left(\frac{\sigma}{r_{\alpha\beta}}\right)^6 \right], \quad \forall \alpha, \beta \in \mathcal{M} \tag{42}$$

with parameters $\varepsilon = 0.467$ eV and $\sigma = 0.2296$ nm is used for the nearest-neighbor interatomic interaction. In the triangular lattice, the equilibrium bond length is $r_0 = 0.2577$ nm and the atomic mass is $m_a = 64$ amu.

The continuum material constants should be consistent with the atomistic model. For this purpose, we use the temperature-related Cauchy–Born rule [47,48] to obtain the continuum constitutive model. Also, thermal conductivity and specific heat capacity at constant strain are calibrated in preliminary fully atomistic simulations. Details of determining continuum material constants are presented in the following.

4.1. Temperature-related Cauchy–Born rule to determine the continuum constitutive model

The Cauchy–Born approximation assumes that the atomic-level lattice follows the deformation given by the macroscopically imposed deformation gradient. The first Piola–Kirchhoff stress tensor can be obtained from the first derivative of the Helmholtz free energy density with respect to the deformation gradient,

$$\mathbf{P}(\mathbf{F}, T) = \frac{\partial \overline{\mathcal{F}}(\mathbf{F}, \mathcal{T})}{\partial \mathbf{F}} \tag{43}$$

in which $\mathbf{P}$ is the first Piola–Kirchhoff stress tensor, $\overline{\mathcal{F}}$ is the Helmholtz free energy density, and $\mathbf{F}$ is the deformation gradient.

Two approximations are adopted to get a useful mathematical form of the free energy for deriving the continuum constitutive models: (1) the quasiharmonic approximation, which uses a harmonic expansion of the potential energy about equilibrium positions and (2) the local harmonic approximation, which neglects coupled vibrations of different atoms in calculation of vibration frequencies of the system. The Helmholtz free energy density is then given as [54,55,47,48]

$$\overline{\mathcal{F}}(\mathbf{F}, T) = \frac{1}{\Omega_u} U(\mathbf{F}, T) + \frac{1}{\Omega_s} k_B T \sum_{\alpha=1}^n \sum_{i=1}^d \text{Ln} \left[2 \sinh \left(\frac{h \omega_{i\alpha}(\mathbf{F}, T)}{4\pi \, k_B T} \right) \right] \tag{44}$$

in which Ω_u is the volume of the unit cell associated with the potential energy, $U(\mathbf{F}, T)$ is the total potential energy in the unit cell, Ω_s is the volume of the unit cell associated with the entropy, n is the number of the atoms in the unit cell associated with the entropy, k_B is the Boltzmann constant, h is the Planck's constant, d is the dimension of the space, and $\omega_{i\alpha}(\mathbf{F}, T)$ is the ith vibration frequency of atom α, which can be obtained from the following equation

$$\left| M_\alpha^A \omega_{i\alpha}^2 \mathbf{I}_{d \times d} - \frac{\partial^2 U}{\partial \mathbf{x}_\alpha \partial \mathbf{x}_\alpha} \right| = 0 \tag{45}$$

where M_α^A is the mass of atom α and $\mathbf{I}_{d \times d}$ is the identity matrix.

The unit cells associated with the potential energy and entropy, used to calculate the Helmholtz free energy density, are shown in Fig. 6. Using these unit cells, the Helmholtz free energy density (Eq. (44)) can be calculated as

$$\bar{F}(\mathbf{F}, T) = \frac{1}{\Omega_u}\left(V_{\alpha\beta} + V_{\beta\gamma} + V_{\alpha\gamma}\right) + \frac{k_B T}{\Omega_s}\sum_{i=1}^{d}\text{Ln}\left[2\sinh\left(\frac{\hbar\omega_{i\eta}(\mathbf{F}, T)}{4\pi k_B T}\right)\right] \tag{46}$$

where $V_{\alpha\beta} = V(r_{\alpha\beta})$, $V_{\beta\gamma} = V(r_{\beta\gamma})$, $V_{\alpha\gamma} = V(r_{\alpha\gamma})$ are the interatomic potentials, given in Eq. (42).

4.2. Preliminary fully atomistic simulations to calibrate thermal conductivity and specific heat capacity at constant strain

To ensure the compatibility between the atomistic and continuum models, continuum thermal properties are calibrated in preliminary fully atomistic simulations. To obtain specific heat capacity at constant strain, an NVT ensemble of 23.4 nm × 23.4 nm with periodic boundary conditions is equilibrated at 300 K and then system temperature is increased to 400 K. The specific heat can be computed as

$$C_{\mathbf{F}} = \frac{1}{V_0}\left[\frac{\partial U}{\partial T}\right]_{\mathbf{F}} = \frac{1}{V_0}\frac{W}{\Delta T} \tag{47}$$

where W is the work done by the thermostat to increase the temperature. Using numerical simulations, we obtained $C_{\mathbf{F}} \approx 5.3 \times 10^5 j/(\text{m}^3 \text{ K})$.

To calibrate thermal conductivity, the atomistic domain, shown in Fig. 7, is used. The right and left boundaries are fixed, and periodic boundary conditions are assumed for the top and bottom boundaries. Two local thermostats maintain the temperature of 300 and 400 K at the left and right ends of the domain, and the rest of the domain is an NVE ensemble. After reaching constant energy flow, system was run for 80 ps and the work done by each thermostat is measured. The work done by two thermostats should have the same absolute values but with opposite signs.

The thermal conductivity can be then computed as

$$K = \frac{q}{\partial T/\partial x} = \frac{W_T L}{A\,\Delta t\,\Delta T} \tag{48}$$

where W_T is the work done by each thermostat in physical time interval Δt, ΔT is the temperature difference between two ends of the domain, and L and A are the length and width of the domain as shown in Fig. 7. Using numerical simulations, we obtained $K \approx 4.2 j/(\text{m K s})$.

4.3. Determination of the meso-mesh size

In the TBDM, the meso mesh is the means to discriminate between thermal vibrations and mechanical deformation. The meso-mesh size, which is independent of the FE-mesh size, should be chosen in a way to resolve all the low-frequency waves whose kinetic energies have negligible effects on temperature. *A priori* numerical tests are used to determine the appropriate mesh size. First, full MD equilibration simulations are conducted on the atomistic domain shown in Fig. 7 at 300 K. The time step was chosen as $\Delta t = 4$ fs and the simulation was run for 50 ps. Then, the numerical simulations were conducted on the same problem domain with a meso-mesh. The temperature was computed using the kinetic energy of only the thermal vibrations, i.e. the waves which cannot be resolved by the meso mesh. Note that in such numerical tests, the meso mesh has no influence on the MD solution, because it is used only as a "cutoff" in computing temperature. The temperature distributions along the x-axis using eleven different meso-mesh sizes are presented in Fig. 8a. It can be seen that the meso-mesh size of 1.069 nm is the optimal meso-mesh size to include all the effective thermal vibrations. Smaller meso-mesh size leads to loss of thermal vibrations, and larger meso-mesh size results in inclusion of mechanical waves which have negligible effect on temperature. Fig. 8b shows the average temperatures over last 20 ps of the simulation using different meso-mesh sizes.
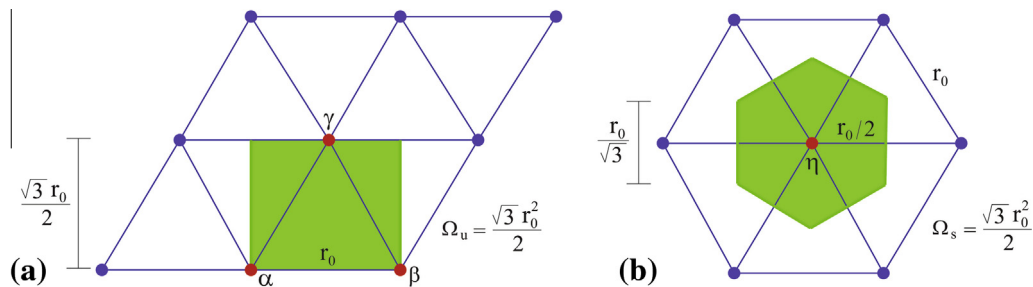

Fig. 6. (a) The unit cell associated with the potential energy, and (b) the unit cell associated with the entropy. Shaded areas denote the unit cells.
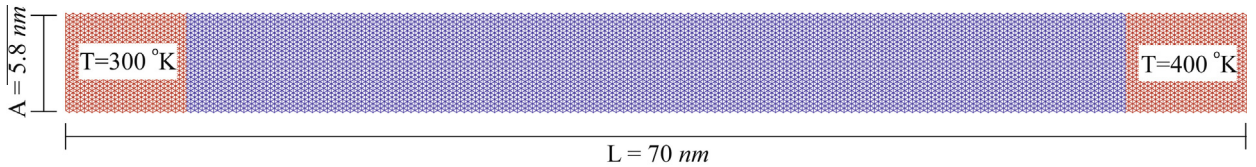
Fig. 7. The full atomistic domain used in the calibration of the thermal conductivity.
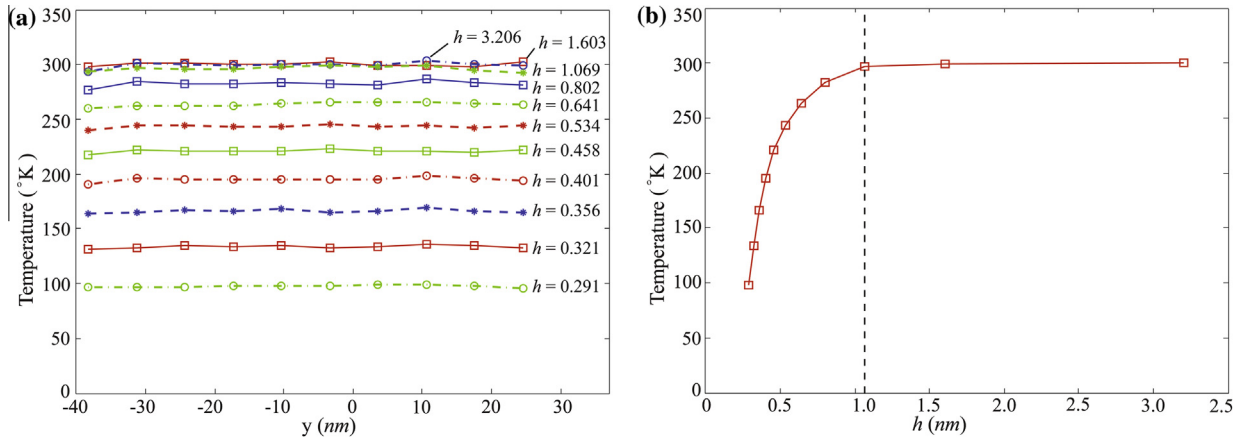

Fig. 8. (a) Temperature distributions along the x-axis by considering 11 different meso-mesh sizes and (b) averaged temperatures over last 20 ps of the simulation using different meso-mesh sizes.

4.4. Equilibration example

The first numerical example is equilibration simulations of full atomistic and multiscale models. The multiscale model, containing 4278 atoms and 14 FE nodes, is shown in Fig. 9. Periodic boundary conditions are assumed for the top and bottom boundaries, and the right and left boundaries are fixed. In the atomistic models, local thermostats are used near fixed boundaries to maintain the boundary temperature and alleviate cooling effects of the fixed boundaries.

The temperature of the FE domain is set to 300 K and the MD domain is thermalized from 0 to 300 K. Time steps are chosen as $\Delta t = 4$ fs and the simulation is run for 50 ps. Time evolution of temperature in the atomistic domain and the temperature distribution along the x-axis, obtained from the multiscale TBDM equilibration simulation, are presented in Fig. 10. As the reference solution, fully atomistic equilibration simulation is also run and the obtained temperature distribution is presented in Fig. 10b. Temperature values presented in Fig. 10b are averaged over last 20 ps of the simulations. Clearly, no cooling effect is observed in the temperature distribution from the multiscale simulation, verifying that indeed the proposed TBDM successfully rectifies the cooling effect of the BD. To verify long-time temperature stability of the proposed algorithm, the multiscale equilibration simulation was run for 1000 ps and no cooling effect was observed.

Also for comparison, the equilibration simulation is re-run using the BDM presented in [25], and the obtained temperature distribution along the x-axis, is presented in Fig. 11. It shows that the BDM suffers from the cooling effect; in addition, application of thermostats does not maintain the target temperatures. This is because the BDM coupling technique damps too strongly the high-frequency atomic vibrations in the BD.

4.5. Heat-transfer example

In this example, the multiscale model used in the previous example (Fig. 9) is subjected to different temperature boundary conditions at its left and right ends. The model is equilibrated for 50 ps at 300 K before the temperate at the right end is
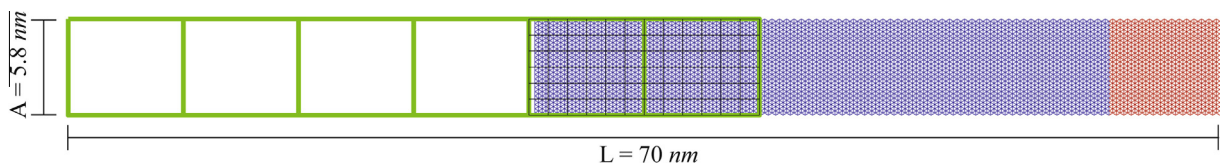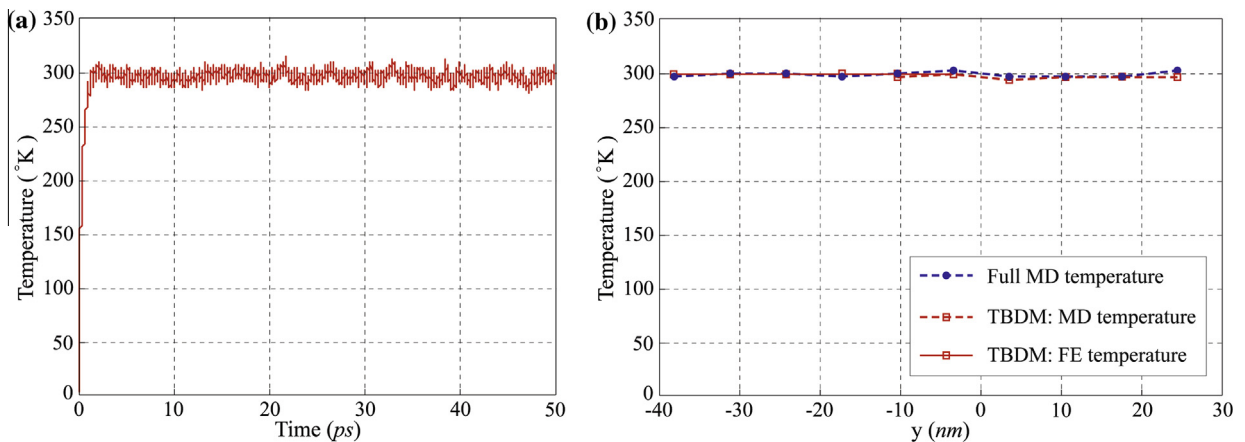

Fig. 9. The multiscale model in numerical simulations.

Fig. 10. (a) Time evolution of temperature in the atomistic domain and (b) the temperature distribution along the x-axis. No cooling effect is observed in the temperature distribution from the multiscale TBDM simulation.
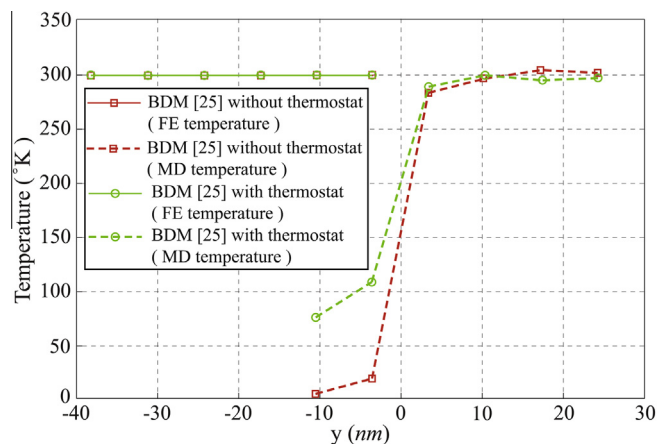

Fig. 11. Temperature distribution along the x-axis, obtained from the equilibration simulation using the BDM [25].

suddenly increased to 400 K. This example is also solved with fully atomistic and fully continuum (FE) models. Temperature distributions along the x-axis, obtained from the TBDM, fully atomistic, and fully continuum simulations, at $t = 10$ ps, $t = 30$ ps, and $t = 90$ ps are depicted in Fig. 12. Temperature values are calculated based on ensemble averaging over 20 ps. Comparing Fig. 12a and b indicates that the multiscale results for the atomistic part are in a good agreement with the results for the same part from the full-atomistic model. Also, comparing Fig. 12a and c shows that the multiscale results for the continuum part are in a good agreement with the full-FE results for the same part.

4.6. Mechanical wave propagation at finite temperature

The multiscale model, shown in Fig. 9, is also used in this example to show that the TBDM accurately transfers low-frequency mechanical deformations between different models while damps out high-frequency mechanical waves, coming out from the MD zone. For this purpose three simulations are run: (1) transferring mechanical deformation from the FE zone to the MD zone, (2) transferring mechanical deformation from the MD zone to the FE zone, and (3) damping out high-frequency mechanical waves, coming out from the MD zone, in the BD. In these simulations, at first, the model is equilibrated for 50 ps at 300 K and then, mechanical wave propagation is simulated.

In the first simulation, the left boundary moves to the left at a constant velocity of 0.05 nm/ps after $t = 50$ ps, and the mechanical deformation is transferred from the FE zone to the MD zone during the simulation. Similarly, in the second simulation, the atoms located at the right boundary move to the right at a constant velocity of 0.05 nm/ps, and the mechanical deformation is transferred from the MD zone to the FE zone. Two snapshots of each of these simulations, showing the horizondal displacements of the atoms and FE nodes along line $y = 0$, at $t = 50$ ps and $t = 70$ ps are depicted in Fig. 13. Fig. 13a and b show that the TBDM accurately transfers mechanical deformation between two models.
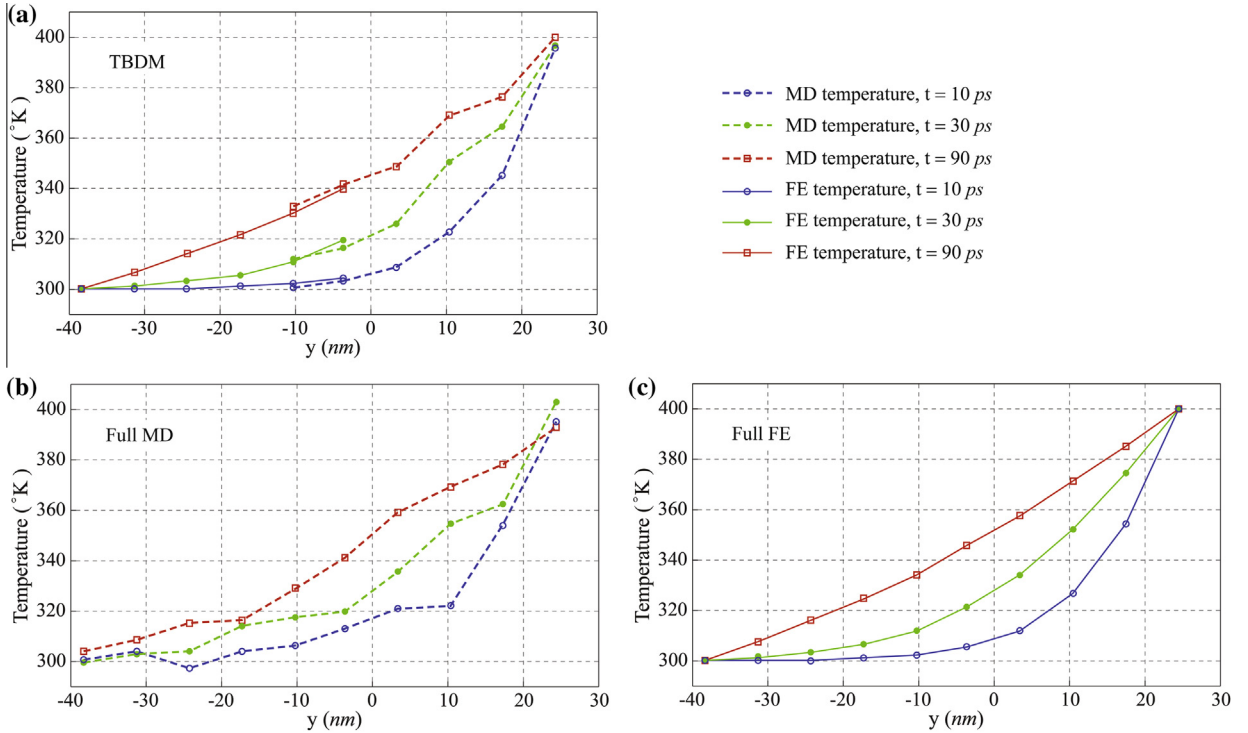
Fig. 12. Temperature distributions along the *x*-axis, obtained from (a) TBDM simulation, (b) full MD simulation, and (c) full FE simulation. The multiscale results are in a good agreement with the full MD and full FE results. Comparing a and b indicates that the multiscale results for the atomistic part are in a good agreement with the results for the same part from the fully atomistic model. Comparing a and c shows that the multiscale results for the FE part are in a good agreement with the full-FE results for the same part.
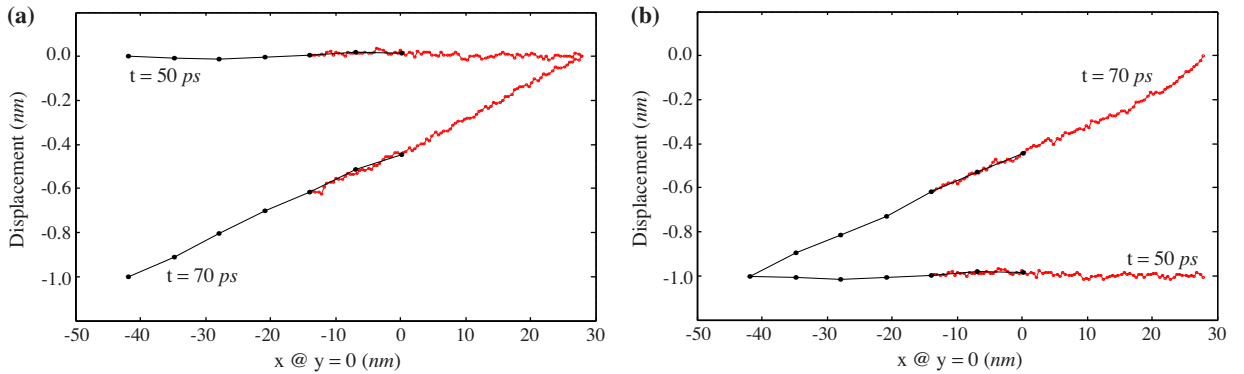

Fig. 13. Snapshots of mechanical deformation simulations, showing the displacements of the atoms and FE nodes along line *y* = 0, at *t* = 50 ps and *t* = 70 ps: (a) transferring the mechanical wave from the FE zone to the MD zone and (b) transferring the mechanical wave from the MD zone to the FE zone.

In the third simulation, a high-frequency mechanical wave, which cannot be resolved by the FE model, is added to the atomic motion at *t* = 50 ps, right after the equilibration. Fig. 14a and b show two snapshots of the multiscale model right before and after adding the mechanical wave, for which the initial displacements and velocities are given by

$$d_{i\alpha}^0 = A\left[1 + \cos\left(2\pi\frac{(X_{i\alpha} + v_w t) - X_{\min}}{X_{\max} - X_{\min}} - \pi\right)\right], \quad i = 1, \ t = 0 \ \text{and} \ X_{\min} \leqslant X_{i\alpha} \leqslant X_{\max} \tag{49a}$$

$$\dot{d}_{i\alpha}^0 = \frac{-2\pi A v_w}{X_{\max} - X_{\min}} \sin\left(2\pi\frac{(X_{i\alpha} + v_w t) - X_{\min}}{X_{\max} - X_{\min}} - \pi\right), \quad i = 1, \ t = 0 \ \text{and} \ X_{\min} \leqslant X_{i\alpha} \leqslant X_{\max} \tag{49b}$$

$$d_{i\alpha}^0 = \dot{d}_{i\alpha}^0 = 0, \quad \text{otherwise} \tag{49c}$$

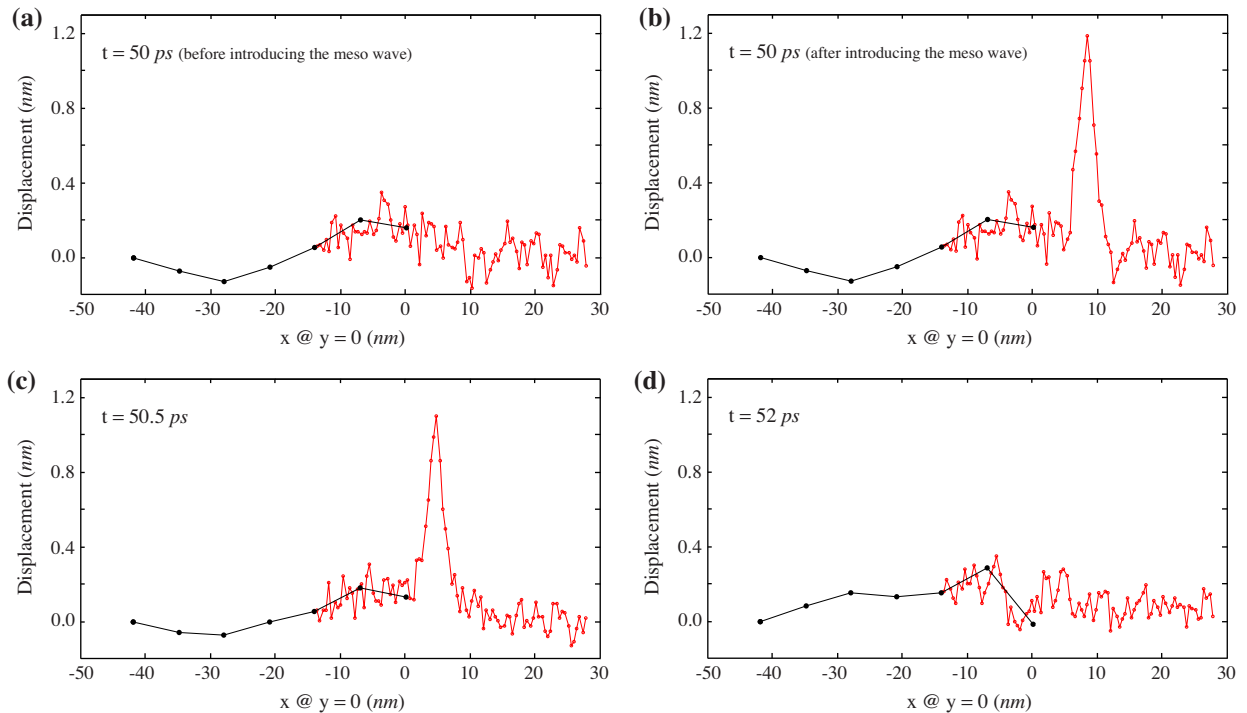where *A* = 0.05 nm, $X_{\min}$ = 5 nm, $X_{\max}$ = 12 nm, and v_w is the wave speed.

Fig. 14. Four snapshots of the high-frequency mechanical wave simulation, showing that the high-frequency mechanical wave, which cannot be resolved by the FE model, is not reflected back to the MD zone.

Two more snapshots of the simulation at t = 50.5 ps and t = 52 ps are depicted in Fig. 14c and d. Fig. 14d shows that the high-frequency mechanical wave, which cannot be resolved by the FE model, is not reflected back to the MD zone. In other words, the proposed TBDM algorithm effectively damps out high-frequency mechanical waves, coming out from the MD zone.

5. Conclusions

Although at zero temperature, a number of materials science problems involving both nonlinear and long-range deformation fields have been successfully simulated by the concurrent multiscale atomistic–continuum methods, improvements are needed to meet challenges unique to finite-temperature simulations. At finite temperature, a successful multiscale method should render atomistic and continuum models thermally compatible, because unlike MD models, continuum models divide the energy into mechanical and thermal components and the system is described by two time-dependent fields, the displacement and the temperature, which are governed by continuum equations of motion and heat equation.

In this paper, an improved BDM is proposed, i.e. the three-layer-mesh BDM (TBDM), which rectifies the recently revealed cooling effect of the original BDM formulation on the atoms in the BD. This is achieved by releasing the constraints between thermal vibrations and FE displacements in the BD. In the TBDM, only the mechanical part of atomic motion is constrained to the FE displacements while unconstrained thermal vibrations are thermostatted using local thermostats in the BD. Specifically, atomic motion in the BD is partitioned into (1) thermal vibrations constituting thermal energy, and (2) mechanical waves contributing to mechanical energy. This partitioning is consistent with the continuum representations and accordingly, each part is separately coupled with the continuum model. A new three-layer mesh structure is introduced in the BD, consisting of coarse, meso and fine meshes, which enables decomposition of total atomic motion into three parts of coarse, meso, and fine scales, so that the coarse and meso parts are quenched to the continuum model using the conventional BDM, and the fine part is thermostatted within the BD using Langevin dynamics. In the TBDM, the meso-mesh size is independent of the FE mesh, which is determined by using a mesh-independent physics-based discrimination between thermal and mechanical waves. The meso part of the atomic motion, which cannot be resolved by the FE mesh and may result in the spurious wave reflection, is suppressed using a damping boundary condition.

Three representative numerical examples demonstrated that (1) the proposed TBDM effectively mitigates the temperature cooling effect encountered by the conventional BDM, (2) the proposed thermal coupling algorithm works well in multiscale heat-transfer simulations, and (3) in multiscale mechanical wave propagation simulations, the TBDM accurately

transfers low-frequency waves between different models while damps out mechanical high-frequency waves, coming out from the MD zone.

We presented the basic formulation of the TBDM and verified its robustness and accuracy by some numerical simulations. We will present application of the TBDM in real-material simulation of graphene sheets using a realistic interatomic potential, the AIREBO potential, in due course.

Acknowledgments

References

[1] A. Ramasubramaniam, E.A. Carter, Coupled quantum–atomistic and quantum–continuum mechanics methods in materials research, Materials Research Society Bulletin 32 (2007) 913–918.
[2] Feng Liu, M.R. Press, S.N. Khanna, P. Jena, Simple theory of electronic structure: clusters to crystals, Physical Review B 38 (1988) 5760–5763.
[3] E.B. Tadmor, M. Ortiz, R. Phillips, Quasicontinuum analysis of defects in solids, Philosophical Magazine A 73 (1996) 1529–1563.
[4] R.E. Miller, E.B. Tadmor, The quasicontinuum method: overview, applications and current directions, Journal of Computer-Aided Materials Design 9 (2002) 203–239.
[5] R.E. Rudd, J.Q. Broughton, Coarse-grained molecular dynamics and the atomic limit of finite elements, Physical Review B 58 (1998) R5893–R5896.
[6] R.E. Rudd, J.Q. Broughton, Coarse-grained molecular dynamics: nonlinear finite elements and finite temperature, Physical Review B 72 (2005) 144104.
[7] F.F. Abraham, J.Q. Broughton, N. Bernstein, E. Kaxiras, Spanning the length scales in dynamic simulation, Computers in Physics 12 (1998) 538–546.
[8] J.Q. Broughton, F.F. Abraham, N. Bernstein, E. Kaxiras, Concurrent coupling of length scales: methodology and application, Physical Review B 60 (1999) 2391–2403.
[9] G.J. Wagner, W.K. Liu, Coupling of atomistic and continuum simulations using a bridging scale decomposition, Journal of Computational Physics 190 (2003) 249–274.
[10] G.J. Wagner, E.G. Karpov, W.K. Liu, Molecular dynamics boundary conditions for periodically repeating atomic lattices, Computer Methods in Applied Mechanics and Engineering 193 (2004) 1579–1601.
[11] T. Belytschko, S.P. Xiao, Coupling methods for continuum model with molecular model, International Journal for Multiscale Computational Engineering 1 (2003) 115–126.
[12] S.P. Xiao, T. Belytschko, A bridging domain method for coupling continua with molecular dynamics, Computer Methods in Applied Mechanics and Engineering 193 (2004) 1645–1669.
[13] J. Fish, M.A. Nuggehally, M.S. Shephard, C.R. Picu, S. Badia, M.L. Parks, M. Gunzburger, Concurrent AtC coupling based on a blend of the continuum stress and the atomistic force, Computer Methods in Applied Mechanics and Engineering 196 (2007) 4548–4560.
[14] S. Zhang, S.L. Mielke, R. Khare, D. Troya, R.S. Ruoff, G.C. Schatz, T. Belytschko, Mechanics of defects in carbon nanotubes: atomistic and multiscale simulations, Physical Review B 71 (2005) 115443.
[15] S. Zhang, R. Khare, Q. Lu, T. Belytschko, A bridging domain and strain computation method for coupled atomistic–continuum modeling of solids, International Journal for Numerical Methods in Engineering 70 (2007) 913–933.
[16] R. Khare, S.L. Mielke, G.C. Schatz, T. Belytschko, Multiscale coupling schemes spanning the quantum mechanical, atomistic force field, and continuum regimes, Computer Methods in Applied Mechanics and Engineering 197 (2008) 3190–3202.
[17] R. Gracie, T. Belytschko, Concurrently coupled atomistic and XFEM models for dislocations and cracks, International Journal for Numerical Methods in Engineering 78 (2009) 354–378.
[18] R. Gracie, T. Belytschko, An adaptive concurrent multiscale method for the dynamic simulation of dislocations, International Journal for Numerical Methods in Engineering 86 (2011) 597–757.
[19] P. Moseley, J. Oswald, T. Belytschko, Adaptive atomistic-to-continuum modeling of propagating defects, International Journal for Numerical Methods in Engineering 92 (2012) 835–856.
[20] G. Anciaux, S.B. Ramisetti, J.F. Molinari, A finite temperature bridging domain method for MD–FE coupling and application to a contact problem, Computer Methods in Applied Mechanics and Engineering 205–208 (2012) 204–212.
[21] H. Ben Dhia, Multiscale mechanical problems: the Arlequin method, Comptes Rendus de l'Academie des Sciences Series IIB Mechanics Physics Astronomy 326 (1998) 899–904.
[22] H. Ben Dhia, G. Rateau, Mathematical analysis of the mixed Arlequin method, Comptes Rendus de l'Academie des Sciences Series I Mathematics 332 (2001) 649–654.
[23] H. Ben Dhia, G. Rateau, Application of the Arlequin method to some structures with defects, Revue Européenne des Éléments 11 (2002) 291–304.
[24] H. Ben Dhia, G. Rateau, The Arlequin method as a flexible engineering design tool, International Journal for Numerical Methods in Engineering 62 (2005) 1442–1462.
[25] A. Sadeghirad, A. Tabarraei, A damping boundary condition for coupled atomistic–continuum simulations, Computational Mechanics 52 (2013) 535–551.
[26] M. Xu, T. Belytschko, Conservation properties of the bridging domain method for coupled molecular/continuum dynamics, International Journal for Numerical Methods in Engineering 76 (2008) 278–294.
[27] W. Cai, M. de Koning, V.V. Bulatov, S. Yip, Minimizing boundary reflections in coupled-domain simulations, Physical Review Letters 85 (2000) 3213–3216.
[28] Weinan E., Z. Huang, Matching conditions in atomistic–continuum modeling of materials, Physical Review Letters 87 (2001) 135501.
[29] Weinan E., Z. Huang, A dynamic atomistic–continuum method for simulation of crystalline materials, Journal of Computational Physics 182 (2002) 234–261.
[30] E.G. Karpov, G.J. Wagner, W.K. Liu, A green's function approach to deriving non-reflecting boundary conditions in molecular dynamics simulations, International Journal for Numerical Methods in Engineering 62 (2005) 1250–1262.
[31] P. Guidault, T. Belytschko, On the L^2 and the H^1 couplings for an overlapping domain decomposition method using Lagrange multipliers, International Journal for Numerical Methods in Engineering 70 (2007) 322–350.
[32] P. Guidault, T. Belytschko, Bridging domain methods for coupled atomistic–continuum models with L^2 or H^1 couplings, International Journal for Numerical Methods in Engineering 77 (2009) 1566–1592.
[33] M. Xu, R. Gracie, T. Belytschko, A continuum-to-atomistic bridging domain method for composite lattices, International Journal for Numerical Methods in Engineering 81 (2010) 1635–1658.
[34] J. Knap, M. Ortiz, Effect of indenter-radius size on Au (001) nanoindentation, Physical Review Letters 90 (2003) 226102.
[35] J. Marian, J. Knap, M. Ortiz, Nanovoid cavitation by dislocation emission in aluminum, Physical Review Letters 93 (2004) 165503.
[36] H. Kadowaki, W.K. Liu, Bridging multi-scale method for localization problems, Computer Methods in Applied Mechanics and Engineering 193 (2004) 3267–3302.

[37] H.S. Park, E.G. Karpov, W.K. Liu, Non-reflecting boundary conditions for atomistic, continuum and coupled atomistic/continuum simulations, International Journal for Numerical Methods in Engineering 64 (2005) 237–259.

[38] H.S. Park, E.G. Karpov, P.A. Klein, W.K. Liu, Three-dimensional bridging scale analysis of dynamic fracture, Journal of Computational Physics 207 (2005) 588–609.

[39] E.G. Karpov, H. Yu, H.S. Park, W.K. Liu, Q.J. Wang, D. Qian, Multiscale boundary conditions in crystalline solids: theory and application to nanoindentation, International Journal of Solids and Structures 43 (2006) 6359–6379.

[40] J. Marian, J. Knap, G.H. Campbell, A quasicontinuum study of nanovoid collapse under uniaxial loading in Ta, Acta Materialia 56 (2008) 2389–2399.

[41] D.J. Diestler, Z.B. Wu, X.C. Zeng, An extension of the quasicontinuum treatment of multiscale solid systems to nonzero temperature, Journal of Chemical Physics 121 (2004) 9279–9282.

[42] L.M. Dupuy, E.B. Tadmor, R.E. Miller, R. Phillips, Finite-temperature quasicontinuum: molecular dynamics without all the atoms, Physical Review Letters 95 (2005) 060202.

[43] J. Marian, G. Venturini, B.L. Hansen, J. Knap, M. Ortiz, G.H. Campbell, Finite-temperature extension of the quasicontinuum method using Langevin dynamics: entropy losses and analysis of errors, Modelling and Simulation in Materials Science and Engineering 18 (2010) 015003.

[44] H.S. Park, E.G. Karpov, W.K. Liu, A temperature equation for coupled atomistic/continuum simulations, Computer Methods in Applied Mechanics and Engineering 193 (2004) 1713–1732.

[45] N. Mathew, R.C. Picu, M. Bloomfield, Concurrent coupling of atomistic and continuum models at finite temperature, Computer Methods in Applied Mechanics and Engineering 200 (2011) 765–773.

[46] S.J. Stuart, A.B. Tutein, J.A. Harrison, A reactive potential for hydrocarbons with intermolecular interactions, Journal of Chemical Physics 112 (2000) 6472–6486.

[47] H. Jiang, Y. Huang, K.C. Hwang, A finite-temperature continuum theory based on interatomic potentials, Transactions of the ASME 127 (2005) 408–416.

[48] S. Xiao, W. Yang, Temperature-related Cauchy–Born rule for multiscale modeling of crystalline solids, Computational Materials Science 37 (2006) 374–379.

[49] P.T. Bauman, H.B. Dhia, N. Elkhodja, J.T. Oden, S. Prudhomme, On the application of the Arlequin method to the coupling of particle and continuum models, Computational Mechanics 42 (2008) 511–530.

[50] M. Luskin, C. Ortner, B. Van Koten, Formulation and optimization of the energy-based blended quasicontinuum method, Computer Methods in Applied Mechanics and Engineering 253 (2013) 160–168.

[51] M. Luskin, C. Ortner, Atomistic-to-continuum coupling, Acta Numerica 22 (2013) 397–508.

[52] B. Van Koten, M. Luskin, Analysis of energy-based blended quasi-continuum approximations, SIAM Journal on Numerical Analysis 49 (2011) 2182–2209.

[53] W. Coffey, Y. Kalmykov, The Langevin Equation: With Applications to Stochastic Problems in Physics, Chemistry and Electrical Engineering, World Scientific Series in Contemporary Chemical Physics, vol. 14, World Scientific Publishing Co. Pte. Ltd., 2012.

[54] D. Chandler, Introduction to Modern Statistical Mechanics, Oxford University Press, USA, 1987.

[55] S. Foiles, Evaluation of harmonic methods for calculating the free energy of defects in solids, Physical Review B 49 (1994) 14930–14938.